

Grain growth competition during melt pool solidification – Comparing phase-field and cellular automaton models

S.M. Elahi^{a,b}, R. Tavakoli^b, I. Romero^{a,b}, D. Tournet^{*b}

^aUniversidad Politécnica de Madrid, E.T.S. de Ingenieros Industriales, Madrid, Spain

^bIMDEA Materials, Madrid, Spain

Abstract

A broad range of computational models have been proposed to predict microstructure development during solidification processing but they have seldom been compared to each other on a quantitative and systematic basis. In this paper, we compare phase-field (PF) and cellular automaton (CA) simulations of polycrystalline growth in a two-dimensional melt pool under conditions relevant to additive manufacturing (powder-bed fusion). We compare the resulting grain structures using local (point-by-point) measurements, as well as averaged grain orientation distributions over several simulations. We explore the effect of the CA spatial discretization level and that of the melt pool aspect ratio upon the selected grain texture. Our simulations show that detailed microscopic features related to transient growth conditions and solid-liquid interface stability (e.g. the initial planar growth stage prior to its cellular/dendritic destabilization, or the early elimination of unfavorably oriented grains due to neighbor grain sidebranching) can only be captured by PF simulations. The resulting disagreement between PF and CA predictions can only be addressed partially by a refinement of the CA grid. However, overall grain distributions averaged over the entire melt pools of several simulations seem to lead to a notably better agreement between PF and CA, with some variability with the melt pool shape and CA grid. While further research remains required, in particular to identify the appropriate selection of CA spatial discretization and its link to characteristic microstructural length scales, this research provides a useful step forward in this direction by comparing both methods quantitatively at process-relevant length and time scales.

Keywords: Solidification, Microstructure, Modeling, Crystal growth Phase-field, Cellular automata, Additive manufacturing

1. Introduction

The formation of grain structures during the solidification of metals and alloys has a crucial effect on the final material properties and the mechanical integrity of structural components. In additive manufacturing (AM), just like in conventional manufacturing processes, grain textures lead to strongly anisotropic material properties [1–5]. The flexibility afforded by AM to locally modulate processing conditions (e.g. through heat source power or velocity) provides a strong motivation for trying to control local microstructure and local mechanical properties of AM components. However, in order to unleash this disruptive potential in fusion-based AM, important gaps remain in our understanding of grain texture selection during solidification in a melt pool.

Grain textures first emerge during grain nucleation and growth competition during the solidification stage. Grain growth competition involves a complex interaction between thermo-solutal conditions and intrinsic

material properties. On the one hand, thermal gradients and growth velocities determine the type of microstructure (e.g. planar, cellular, dendritic). On the other hand, the intrinsic crystalline structure dictates solid-liquid interface anisotropy and preferred growth directions. Early theories considered that grains with their preferred growth direction ($\langle 100 \rangle$ in most cubic crystals) best aligned with the main temperature gradient direction had to be favored in the growth competition against neighboring grains with higher misorientation to the temperature gradient [6]. While this is, on average, considered to be true, later experimental observations highlighted more complicated growth competition mechanisms that did not follow this simple picture [7–9]. Recent computational studies [10–13] have provided major advances into the fundamental understanding of grain growth competition mechanisms, focusing on idealized temperature conditions, namely with a one-dimensional temperature gradient.

Deviations from such an idealized thermal field may have important consequences on selected microstructures. For instance, in directional (Bridgman) solidification, a small curvature of the isotherms due to lateral

*Corresponding author; Email address: damien.tournet@imdea.org

heat extraction [14] or a global shift of the isotherms due to thermal inertia of the experimental setup [15], may lead to strong differences in microstructures, e.g., leading to the lateral drift of cellular/dendritic patterns and heterogeneities in the selected primary spacings [15, 16], which strongly affects the dynamics of grain growth competition [16]. Yet, these deviations from a one-dimensional temperature field are often neglected in fundamental studies of polycrystal growth, which often use idealized temperature fields, e.g. the classical frozen temperature approximation [10–13, 16]. One objective of the present study is to perform simulations of polycrystalline solidification within a multi-dimensional thermal field relevant to AM, in order to analyze the mechanisms of grain growth competition in a melt pool.

While experimental studies of carefully controlled bicrystal growth competition are possible [17–20], they remain challenging to perform. Meanwhile, quantitative simulations of solidification have emerged that allow thorough studies of microstructure selection while exploring individual parameters – e.g. crystal orientations, temperature gradients, and cooling rates – independently. A host of models for solidification have been developed using a broad palette of numerical methods, including front tracking [21, 22], Monte Carlo [23, 24], phase-field-crystal [25], level set [26, 27], grain envelope [28–30], needle network [31, 32], cellular automaton [33, 34], and phase-field [35, 36] approaches. In this study, we focus on cellular automaton and phase-field methods, which are by far the most utilized approaches for simulating grain structure predictions in solidification, to a great extent due to their generality and simplicity.

At the scale of individual dendrites or dendritic arrays, phase-field (PF) is an outstanding method for simulating the evolution of morphologically complex interfaces based only on thermodynamics and kinetics considerations [35–37]. The PF method has proven especially successful in the field of solidification, where “mesoscale” formulations have been developed that remain faithful to the sharp-interface problem even for diffuse interfaces much wider than the actual interface width [38, 39]. However, the spatial discretization required for well-converged quantitative simulations is intrinsically limited by the microstructural length scale, i.e. the local interface curvature [37, 39, 40]. These limitations can, to some extent, be alleviated using advanced implementations, e.g. using massive parallelization on graphics processing units (GPUs) [41], but resulting simulations remain computationally expensive. We have recently shown that well-converged PF simulations of polycrystalline solidification in AM-relevant conditions could be achieved at the scale of the entire melt pool in two dimensions (2D) [42]. Yet, even though the resulting simulation was performed using reasonable computing resources (one node equipped

with eight Nvidia GPUs), such simulations remain quite challenging computationally (e.g. involving over one billion grid points).

At the larger scale of entire grain structures or even entire components, cellular automaton (CA) models provide a good compromise between efficiency and physics-based considerations [33, 34, 43–48]. In CA models, grains are constructed from polyhedral building blocks, whose vertices mark the preferred crystallographic growth directions. Growth velocities in these directions follow simplified, yet physics-based, kinetic laws for crystal growth – e.g. using Ivantsov-based relations or power laws relating local supersaturation or undercooling [49, 50]. As such, CA models include more adjustable phenomenological parameters than PF models. The significant computational advantage – and hence upscaling potential – of CA over PF resides in their relatively much coarser spatial discretization. Advanced schemes have been developed to couple CA with macroscopic thermomechanical solvers, e.g. using finite elements (FE) [34, 43, 45, 48, 51], thus enabling the combination of solidification thermodynamics and kinetics (CA) with macroscopic transport of heat, solute and mechanics (FE). Notably, CA with finer grid sizes have also been used to simulate the growth of individual dendrites [52–55]. However, additional terms are required to capture the effect of local interface curvature, and the cell size needed to appropriately represent dendrite tips somewhat reduces their computational advantage.

A key motivation for the development of CA models for solidification in the 1990’s was specifically the prediction of grain textures via grain growth competition [56–59]. Early articles suggested that the appropriate length scale for the typical CA cell size (h_{CA}) was the secondary dendrite arm spacing [60]. However, until recently [61, 62], the effect of h_{CA} on the predicted grain growth competition, and its link to microstructural length scales, was not carefully studied. As a result, the grid size has often been selected as an adjustable parameter based principally on numerical convenience. Recent studies [61, 62] have shown that CA simulations lead to results closest to PF when h_{CA} is of the same order as the “height” (undercooling) difference between the two competing grains within the temperature gradient [61] or comparable to the active secondary dendritic spacing within competing grains [62]. These studies remain to be extended to polycrystalline microstructures in multi-dimensional temperature fields. A key objective of the present study is the quantitative comparison of PF and CA predictions of grain structures in AM-relevant conditions, performed over a statistically significant number of grains, in order to assess the effect of h_{CA} and provide further guidelines for its selection.

Hence, in this paper, we compare directly and quantitatively the grain structure predicted by PF and CA

models for similar thermal conditions relevant to AM. We perform these calculations in two dimensions, but at the entire melt pool scale, and repeat most of them several times with different initial grain structures, in order to obtain a statistically meaningful picture of grain growth competition in a two-dimensional temperature field. In particular, these results allow us to discuss (1) the mechanisms of unsteady dendritic grain growth competition in an AM-relevant 2D thermal field, (2) the advantages, but also the limitations of upscaling PF simulations using CA, and (3) the appropriate choice of cell size for a reasonable matching between CA and PF predictions.

2. Methods

With the objective to compare PF and CA simulations of melt pool solidification, we consider material and laser properties from a previous study on powder-bed fusion of Inconel 718 alloy [42]. Therein, temperature-dependent alloy properties — namely heat capacity, density, thermal conductivity — are calculated using the CalPhaD method (ThermoCalc, TCNI8 database) or tabulated from experimental literature. The steady-state thermal field in the melt pool region is calculated using finite elements (FE), as described with detail in Ref. [42]. We use the resulting three-dimensional (3D) thermal field to extract two-dimensional sections, namely longitudinal and transversal, which we use as the temperature field in either PF or CA simulations. In the subsequent simulations of solidification, we use alloy properties and phase diagram for a binary Ni-5wt%Nb alloy given in Ref. [42]. Importantly, we consider that solidification occurs solely by epitaxial growth from the bottom of the melt pool, and neglect nucleation, thus focusing on the growth competition and avoiding the addition of further adjustable parameters (e.g. nuclei density and nucleation undercooling).

The restriction to 2D simulations of polycrystalline solidification is arguably a limitation. However, previous studies have shown that grain growth competition mechanisms are appropriately reproduced by 2D simulations when compared to quasi-2D three-dimensional simulations [13]. Hence, even though the full space of 3D orientations cannot be scanned in these 2D simulations, we still expect that they should be able to capture — even if only qualitatively — phenomena such as the grain texture transition as a function of the melt pool aspect ratio [63, 64]. Conceptually, both PF and CA models used here are readily applicable in three-dimensions [13, 43]. However, the fine spatial discretization required for PF simulations (here of order 5 to 10 nm) prevents the execution of dendrite-resolved quantitative simulations in 3D at the scale of the entire melt pool, even using massive computational resources (already requiring over a billion grid points in

the current longitudinal section simulation [42]). From the CA perspective, full melt pool and even multi-pass simulations are achievable [43]. However, except for bicrystalline 2D simulations in a one-dimensional temperature field [42, 61], the accuracy of CA simulations of polycrystalline grain growth competition in AM-relevant conditions has not been addressed to date — which is a key objective of the current article.

2.1. Thermal field

Based on the results of 3D FE, we extract 2D longitudinal (i.e. within a horizontal plane that contains the heat source location and its path) and cross sections (i.e. within a horizontal plane normal to the scanning direction) of the temperature field in the melt pool region. Then, we approximate the temperature field, T , with simple analytical formulae that consider an elliptical shape of liquidus and solidus isotherms.

In terms of grain growth competition during solidification, the most important region, where the temperature field needs to be described accurately enough, is between the solidus ($T_S = 1554$ K) and liquidus ($T_L = 1625$ K) temperatures. Therefore, the analytical fitted functions are chosen to obtain a reasonable description of the time-dependent location of ($T = T_L$) and ($T = T_S$), and hence of the temperature gradient in the freezing range, regardless of the approximation accuracy below T_S or above T_L .

2.1.1. Longitudinal section

The analytical approximation of the thermal field longitudinal section is similar to that used and discussed in Ref. [42]. Specifically, the temperature field is defined in polar coordinates through the function

$$T(r, \theta) = T_L + (T_0 - T_L) \frac{r - r_L(\theta)}{r_S(\theta) - r_L(\theta)}, \quad (1)$$

where $r_S(\theta)$ and $r_L(\theta)$ are respectively the radii of the location of solidus and liquidus isotherms at a given angle $\theta = \tan^{-1} |(y - y_0)/(x - x_0)|$, where (x_0, y_0) is the location of the center of the ellipses, and $r = \sqrt{(x - x_0)^2 + (y - y_0)^2}$. The solidus and liquidus isotherms are modeled as two ellipses with

$$r_L(\theta) = \sqrt{\frac{(l_L d_L)^2}{(d_L \cos(\theta))^2 + (l_L \sin(\theta))^2}}, \quad (2)$$

$$r_S(\theta) = \sqrt{\frac{(l_S d_S)^2}{(d_S \cos(\theta))^2 + (l_S \sin(\theta))^2}}, \quad (3)$$

with (l_L, l_S) the lengths and (d_L, d_S) the depths of solidus (subscript S) and liquidus (L) isotherms, respectively. The resulting temperature field T is shifted in the direction x with the velocity of the laser beam $V_L = 0.1$ m/s.

2.1.2. Cross-section

The cross-section temperature is also approximated using elliptical solidus and liquidus isotherms, which shrink non-linearly with time, in order to provide a reasonable fit to the FE results. In this case, the temperature is interpolated linearly between the temperature at the center of the melt pool T_0 and the solidus temperature T_S as

$$T(r, \theta) = T_0(\theta, t) + (T_S - T_0(\theta, t)) \frac{r}{r_S(\theta, t)}, \quad (4)$$

with the location of the solidus temperature isotherm given by the equation of an ellipsis

$$r_S(\theta) = \sqrt{\frac{(w_S(t) d_S(t))^2}{(d_S(t) \cos(\theta))^2 + (w_S(t) \sin(\theta))^2}}. \quad (5)$$

The time-dependent half-width w_S and depth d_S of this isotherm are described by

$$w_S(t) = w_0 [1 - (t/t_f)^{n_w}], \quad (6)$$

$$d_S(t) = d_0 [1 - (t/t_f)^{n_d}], \quad (7)$$

where w_0 and d_0 are the initial (i.e. maximal) half-width and depth of the melt pool, and t_f is a time at which both w_S and d_S reach zero. The time evolution of w_S and d_S between $(w_S, w_L) = (w_0, d_0)$ at $t = 0$ and $w_S = w_L = 0$ at $t = t_f$ is parametrized using exponents n_w and n_d (linear evolution if exponent equals 1, or late and steep evolution for higher exponents). Parameter values $w_0 = 128 \mu\text{m}$, $d_0 = 96 \mu\text{m}$, $t_f = 0.00255 \text{ s}$, $n_w = 20$, $n_d = 3$ are adjusted for a good fit to the FE results (see Supplementary Material – Section A – Fig. A.2.a).

The time evolution of the temperature at the center of the melt pool $T_0(\theta, t)$ is described in order to provide a reasonable location of the liquidus temperature location by radial interpolation between $T_0(\theta, t)$ at $r = 0$ and T_S at $r = r_S$. For our specific FE results, at the early stage of melt pool shrinking, $T_0(\theta, t)$ is well described by a θ -dependent function

$$T_1(\theta) = T_w - (T_w - T_d) \sin(\theta), \quad (8)$$

where T_w and T_d are values of T_0 extrapolated radially from the location of T_S and T_L along the width and depth, respectively, and using a simple sine interpolation between T_w and T_d along θ . At the later stage of the melt pool shrinking, $T_0(\theta, t)$ is well described by a time-dependent function

$$T_2(t) = T_L - R(t - t_L), \quad (9)$$

where R is a constant cooling rate and t_L is an approximate time at which T_0 approaches T_L (see Supplementary Material – Section A – Fig. A.2.b). Between early and late stages, $T_0(\theta, t)$ is interpolated in time between $T_1(\theta)$ and $T_2(t)$ using a sigmoid (hyperbolic tangent) function

$$T_0(\theta, t) = \frac{T_1(\theta) + T_2(t)}{2} - \frac{T_1(\theta) - T_2(t)}{2} \tanh\left(\frac{t - \tau(\theta)}{\sigma(\theta)}\right), \quad (10)$$

in which the time and duration of the sigmoid transition from T_1 to T_2 are parametrized using

$$\tau(\theta) = \tau_w - (\tau_w - \tau_d) \sin(\theta), \quad (11)$$

$$\sigma(\theta) = \sigma_w - (\sigma_w - \sigma_d) \sin(\theta). \quad (12)$$

Here, τ_w and σ_w correspond to optimal values along the width ($\theta = 0$), whereas τ_d and σ_d are optimal values along the depth ($\theta = \pi/2$), interpolated along θ using a simple sine function. Parameter values $T_w = 2700 \text{ K}$, $T_d = 2450 \text{ K}$, $R = 1.2 \times 10^5 \text{ K/s}$, $t_L = 0.00195 \text{ s}$, $\tau_w = 0.00115 \text{ s}$, $\tau_d = 0.0007 \text{ s}$, $\sigma_w = 0.00036 \text{ s}$, and $\sigma_d = 0.0005 \text{ s}$ were found to provide a good match to our FE results in terms of liquidus ($T_L = 1625 \text{ K}$) and solidus ($T_S = 1554 \text{ K}$) isotherms and their time evolution (see Supplementary Material – Section A – Fig. A.3).

The temperature field given by Eq. (4) is arguably approximate and has a high number of adjustable parameters, which may even lead to singularities if not chosen carefully. As such, it is not intended to provide a general description of melt pool temperature fields. A direct use of a tabulated FE-calculated field using an efficient interpolation scheme could have been a more accurate choice. However, this analytical approximation still provides a reasonable analytical description of the FE-calculated temperature field (see Supplementary Material – Section A), which is more than sufficient for our study of grain growth competition.

2.1.3. Explored thermal configurations

We simulate one configuration for the longitudinal section, similar to that presented in Ref. [42] and 15 different cross-section configurations, as summarized in Table 1. For the latter, we consider three melt pool shapes: (1) one corresponding to the original fit to the FE results (i.e. using equations and parameters listed in Section 2.1.2), (2) one with a twice wider and twice shallower melt pool (i.e. with $w_0 = 256 \mu\text{m}$, $d_0 = 48 \mu\text{m}$), and (3) one with a twice deeper and twice narrower melt pool (i.e. with $w_0 = 64 \mu\text{m}$, $d_0 = 192 \mu\text{m}$). For each of these three melt pool shapes, we consider five initial configurations with different randomly generated initial grain maps.

Table 1: Thermal configurations for cross-section simulations.

Configuration	Domain Size ($\mu\text{m} \times \mu\text{m}$)	w_0 (μm)	d_0 (μm)
Reference	257×97	128	96
Wide & Shallow	513×49	256	48
Deep & Narrow	129×193	64	192

2.1.4. Initial grain structures

To build these initial grain maps, a total of 1500 grain centers are generated at random locations using a Poisson disk sampling algorithm. A random orientation, namely an integer in the range $[1 - 90]$, is attributed to each grain center. This integer grain index is then used as the crystalline orientation, in degrees, of the grain with respect to the computational grid frame of reference. After the Voronoi tessellation step that propagates the orientation of each center to its corresponding polygonal grain, the grid points with temperature above T_L , which belong to the melted region, are reinitialized to the liquid state and their grain orientation is “erased”. Solidification calculations for the sixteen configurations are carried out once with PF simulations (Section 2.2) and several times with different grid element sizes with CA simulations (Section 2.3). It should be noted that the Voronoi-based initial structures are used for simplicity and generality but not intended to represent a realistic AM microstructure – e.g. from previous layer building – but rather used as a test case to compare PF and CA predictions in identical configurations.

2.2. Phase-Field

The PF model used here is similar to that described in Ref. [42]. It is a classical quantitative PF model for dilute binary alloy solidification [39] with nonlinearly preconditioning of the phase field [11, 65] considering an externally imposed temperature field [42]. The solid-liquid interface is assumed to be at equilibrium. Neglecting solute trapping restricts its application to a low-to-moderate interface velocity relevant to the lower velocity range experience in powder-bed fusion processes. For the considered laser velocity $V = 0.1$ m/s, the interface remains in the appropriate velocity range to neglect any significant solute trapping effects (see discussion in Ref. [42]). Furthermore, the velocities of isotherms along the cross-section are even lower than those in the longitudinal section [66]. We use a simple polycrystalline extension of the model [42] which does not consider any solid-solid motion of the grain boundaries (GB) once formed. This assumption neglects any further coarsening of the microstructure, e.g. during the intrinsic heat treatment experienced by the microstructure during the deposition of upper layers. However, here we chose to focus primarily on the epitaxial growth and grain growth competition of

columnar grains with different crystal orientations in the melt pool.

All boundary conditions are set to no-flux on both solute and phase fields. The longitudinal section simulation, presented in Ref. [42], considers a moving frame advancing with respect to the material at the velocity of the laser, hence conserving a temperature field given by Eq. (1) fixed within the computational domain. On the other hand, the cross-section simulations consider a fixed frame with respect to the material and a shrinking melt pool according to Eq. (4).

Phase-field equations are solved with a fully explicit first order in time and second order in space finite difference method on a uniform grid. A grid spacing $h_{\text{PF}} = 5$ nm is used for the spatial discretization for the longitudinal section simulations, following the convergence study performed in Ref. [42]. In the cross-section simulations, the solid-liquid interface velocities are lower, such that a coarser discretization can be afforded with $h_{\text{PF}} = 10$ nm. The time step size is taken to be equal to 0.3 of the stability limit for Laplacian operators. With the exception of the grid spacing h_{PF} , the initial grain distributions, and the thermal field (Section 2.1), all parameters are identical to those used in Ref. [42].

2.3. Cellular Automaton

We implemented a standard 2D cellular automaton model to track the envelope of grains [33, 34, 60]. The model uses a uniform grid with a cell size h_{CA} . Each cell is associated with a growing polygon whose vertices are oriented toward the $\langle 100 \rangle$ ($\langle 10 \rangle$ in 2D) crystalline directions of the grain and grow at a velocity calculated from the local undercooling. When the polygon grows enough to capture the center of neighboring cells, the captured cell is activated and its own associated polygon is initialized and starts to grow.

We considered an eight-neighbor (Moore) capture and a classical decentered square algorithm [44, 51, 60, 67]. More advanced algorithms exist that may be more accurate in presence of a high temperature gradient, e.g. considering irregular (kite-shaped) quadrangles accounting for the different local velocities of the individual vertices [58, 61, 68, 69]. However, we chose the decentered square method as it is one of the most widely used due to its simplicity, in particular in recent applications to additive manufacturing [44, 46, 48], while the approach still reduces grid-induced anisotropy and appropriately captures non-uniform temperature fields [60].

The CA model and algorithm are essentially identical to those of Refs [44, 60]. We verified our algorithm against the analytical result of a tilted grain growing in a temperature gradient, i.e. specifically reproducing the results of Fig. 2 in Ref. [60].

The growth velocity of the square vertices, V , was estimated using

$$V_{\text{KGT}} = 6.45 \times 10^{-8} \times \Delta T^{3.83} + 5.71 \times 10^{-6} \times \Delta T^{1.98}, \quad (13)$$

where the undercooling $\Delta T = T_L - T$ is measured at the center of the cell. The coefficients and exponents of Eq. (13) were adjusted to approximate the results of the classical Kurz-Giovanola-Trivedi model [50] at $V < 0.1$ m/s using parameters of the Ni-5wt%Nb considered in the PF simulations.

For simplicity, all CA simulations consider a frame fixed to the material and an evolving temperature field following either Eq. (1) with $x_0(t) = x_0(0) + V_L \times t$ or a shrinking melt pool following Eq. (4). All other alloy properties, processing parameters, and boundary conditions are similar to that used in the PF simulations.

The selected CA algorithm has two major computational advantages over the PF method: (1) the CA model relies exclusively on the temperature field and does not require tracking of the solute concentration field, and (2) the individual cell size h_{CA} used in the CA can be chosen to be much coarser than that required for accurate PF simulations (typically an order of magnitude smaller than the dendrite tip radius [39, 40]). However, as mentioned in Section 1, strategies for the appropriate choice of numerical parameter h_{CA} remain unclear. Hence, here we aim at addressing two key questions:

- To what extent can a CA reproduce PF predictions of grain growth competition in a polycrystalline unsteady 2D temperature field?
- What is an appropriate element size for the CA grid, or otherwise stated, above which value of h_{CA} do CA predictions start deviating significantly from reference results at low h_{CA} ?

Therefore, for each configuration (one longitudinal, fifteen cross-sections), we perform CA simulations using different h_{CA} and quantitatively compare the resulting grain maps with one another and with PF results (see Section 2.4). We explore values of h_{CA} with a ratio $h_{\text{CA}}/h_{\text{PF}}$ between 6 and 1152 for the longitudinal section ($h_{\text{PF}} = 5$ nm) and between 3 and 144 for the cross-section ($h_{\text{PF}} = 10$ nm) simulations.

2.4. Post-processing

We seek a quantitative comparison of CA and PF results on the basis of resulting grain maps and overall grain textures. We also want to explore the potential transition of favored grain texture in the melt pool as a function of the melt pool shape.

In order to compare PF and CA grain maps, since we use a cell size h_{CA} that is systematically a multiple of the PF grid element size h_{PF} we can artificially refine the CA results to a grid similar to that of the PF. To

do so, we attribute the grain orientation of a given cell to all points of the refined grid included within each CA cell. We can then compare the two grids of similar size by counting the number of points within the melt pool that have a similar or different grain orientation.

We define a region of measurement that includes only the melted region, in order to discard the unmelted Voronoi grain distribution at the bottom or sides of the domain. In the longitudinal simulation, we also exclude the upper region of the domain, which may be affected by the boundary conditions, namely excluding the upper $10 \mu\text{m}$ at the top of the simulation from the measurement region. Within the resulting region, denoted Γ , we count the number of grid point $(i, j) \in \Gamma$ in which the grain orientation differs between CA and PF, which we then normalize by the total number of grid points in Γ . This way, we obtain a difference metric (in area fraction) that is equal to 0 if the grain maps are exactly the same and 1 if all grid points differ in the considered region Γ .

We also extract overall grain orientation distribution within each melt pool, within the same melted region Γ . We only perform this analysis on the cross-section simulations, which present a higher degree of statistical relevance with five different simulations performed for each configuration. The grain distributions are simply extracted as the number of grid points of a given orientation, combined over the five runs for each configuration, and then binned into orientation ranges of width 9° and centered on $0^\circ, 9^\circ, 18^\circ \dots 90^\circ$ (the last bin centered on 90° being the same as that centered on 0°).

In order to correlate the grid element sizes to physical length scales of the microstructure, we also extract values of primary and secondary arm spacings within the PF-simulated microstructures. To do so, we perform line scans on the solute composition field (similar to those presented in Fig. 9 of Ref. [42], where scans A, B, C, and E correspond to primary spacings and scan D corresponds to secondary spacings) in large grains presenting the clearest primary or secondary spacings. From there, the estimation of the spacing is straightforward from locating the first and last concentration peaks (corresponding to interdendritic regions) and counting the number of spacings in between. The resulting average spacings correspond to a total of 63 primary and 159 secondary measured spacings in the longitudinal simulation, and a total of 196 primary and 388 secondary measured spacings in the cross-section simulations. We did not estimate secondary spacings in the shallow melt pools that were composed principally of primary dendrites, and we averaged the primary (λ_1) and secondary (λ_2) spacings over the different melt pools sizes, as we did not see any significant differences between melt pool shapes.

3. Results and discussions

3.1. Computational performance

Phase-field simulations were parallelized on multiple graphics processing units (GPUs) [42]. The resulting longitudinal section simulation had over one billion grid points ($50\,000 \times 20\,000$) iterated over 6.6 million time steps, and was performed in less than 10 days using eight Nvidia RTX 2080Ti GPUs. The cross-section simulations considered different melt pool sizes (see Section 2.1.3) and hence different grid sizes ($12\,900 \times 19\,300$, $25\,700 \times 9\,700$, and $51\,300 \times 4\,900$). Each of them has approximately 250 million grid points iterated over 858 thousand time steps, corresponding to a physical simulated time of 2.6 ms. The simulations were performed on various Nvidia GPU models, most of them using two RTX3090 GPUs. All simulations performed with two RTX3090 GPUs were completed in less than 44h (wall time). The observed strong scaling with the number of GPUs is nearly linear ($\pm 10\%$).

As expected, the coarser CA grid relative to PF simulations leads to a substantial computational advantage. Instead of using multiple parallel GPUs as in PF simulations, each CA run was performed on a single Intel Xeon 6130 CPU core (2.10 GHz). For the longitudinal section simulation, compared to the 10 days using eight GPUs (PF), the CA simulations were completed in 30 seconds or less (for $h_{CA}/h_{PF} \geq 192$) and up to 10.5 days (for $h_{CA}/h_{PF} = 6$). Typical simulations with an intermediate grid, e.g. with $h_{CA}/h_{PF} = 24$, last about 4 hours. As for the cross-section simulation, compared to the 44h using two GPUs (PF), the CA simulations with the reference melt pool size were completed in between a few seconds ($h_{CA}/h_{PF} = 144$) and 4 days ($h_{CA}/h_{PF} = 3$). Simulations with an intermediate grid, with $h_{CA}/h_{PF} = 24$, last about 11 minutes. Computational times for all configurations are listed in the joint Supplementary Material (Section C).

3.2. Longitudinal section

Figure 1 shows the difference, in area fraction, between CA and PF grain maps, in the measured area Γ , for different CA grid sizes. The measured primary and secondary arms spacings, respectively $\lambda_1 = 1.26 \mu\text{m}$ and $\lambda_2 = 1.03 \mu\text{m}$, are also reported as vertical lines.

Several important observations emerge from Fig. 1. First, the difference between CA and PF is essentially increasing as the CA grid gets coarser, and the CA results seem to converge to a plateau as h_{CA} is reduced. However, even the best results for a well-converged CA, reached for approximately $h_{CA} \leq 0.2 \mu\text{m}$ (i.e. $h_{CA}/h_{PF} \leq 40$), still show over 40% of difference with PF. This h_{CA} is significantly lower than the measured dendrite arm spacings $\lambda_1 = 1.26 \mu\text{m}$ and $\lambda_2 = 1.03 \mu\text{m}$. This monotonic behavior contrasts with previous results in bi-crystal configurations [61, 62], which have

shown that a minimum can be found somewhere between the so-called *geometrical limit* (at low h_{CA}) and the *favorably-oriented grain* (at high h_{CA}) asymptotic behaviors. At the highest h_{CA} , the CA prediction fails over more than 90% of the solidified area, as the cell size becomes comparable to the grain size. From these results, while the most appropriate choice for the CA grid size seems to be toward low h_{CA} , which leads lower difference with PF, the correlation with microstructural length scales remains unclear and requests further investigation.

We also explored the effect of some key features of the CA model on these results, such as the neighborhood considered for cell captures, as well as the growth law considered for the dendrite tips (i.e. square vertices). Changing the capture neighboring algorithm from Moore (eight neighbors, used as default here) to von Neumann (four neighbors) definition does not affect the results substantially.

Regarding the growth velocity, we find that increasing the growth velocity (by multiplying V from Eq. (13) by a factor 10) or decreasing it (dividing by a factor 10) has a relatively limited effect, at least in this specific example. However, such conclusion needs to be taken carefully, keeping in mind that we are here in presence of a relatively high temperature gradient. One main effect of a higher $V(\Delta T)$ is that the solidification front (dendrite tips) will be located closer to the liquidus temperature, stabilizing at a relatively lower ΔT for the same V , while a lower $V(\Delta T)$ will promote a stabilization of the solidification front deeper in the mushy zone (closer to the solidus temperature). Due to the high temperature gradient considered here, between 10^6 at the bottom and 10^7 K/m at the tail of the melt pool (See Ref. [42], Fig. 5 therein), the solidus and liquidus isotherms are relatively close to

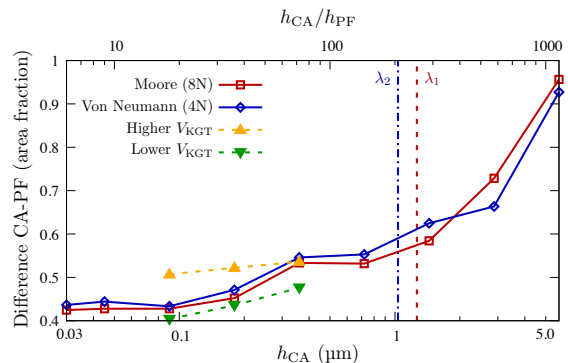


Figure 1: Difference between orientation maps in CA and PF results, as a fraction of the measured area Γ , considering CA results using either Moore (eight-neighbor) or von Neumann (four-neighbor) neighborhood, as well as artificially higher ($V = 10 \times V_{KGT}$) or lower ($V = V_{KGT}/10$) growth velocities, i.e. respectively multiplying or dividing the right-hand side of Eq. (13) by a factor of 10. Vertical lines show the measured values of primary (λ_1) and secondary (λ_2) dendrite arm spacings.

each other, which minimizes the effect of $V(\Delta T)$.

Figure 2 shows the resulting grain maps in the longitudinal section for the well-converged ($h_{PF} = 5\text{ nm}$) PF simulation, as well as for three different levels of CA grid size, namely $h_{CA}/h_{PF} = 9, 48,$ and 288 . We did not analyze quantitatively the average grain distributions in the melt pool, because the number of grains in this single simulation does not provide a sufficient sample size for statistically meaningful results. Still, the overall distribution of grains appears close in most simulations, with a grain orientation, i.e. a preferred growth direction α measured counterclockwise from the horizontal $x+$ direction, close to 60° (predominantly shades of green) in most of the melt pool, and closer to 45° (orange) around the tail of the melt pool. However, the PF simulation shows a broader distribution of orientations with some large grains at $\alpha \approx 15^\circ$ (purple), 30° (red), and 0° (blue), which are much less present in CA-predicted grain maps.

Figure 3 provides a more detailed view of three regions labelled A, B, and C in Fig. 2. The underlying dendritic structures overlaid on the PF grain map allows to identify the mechanism of grain growth competition at play at each GB (namely impingement at converging GBs and sidebranching at diverging GBs [11]) and to better understand the agreements and differences between PF and CA predictions.

Region A, located close to the tail of the melt pool, illustrates a region of good agreement between PF and

CA, nearly regardless of the CA grid. Most grain boundaries are of converging type, except for diverging GB 4 – 5. Considering that the main direction of the temperature gradient is normal to the fusion line (marked in dashed black line), the preferred growth orientation is close to $\alpha \approx 45^\circ$. As a result, all converging GBs in this region follows the favorably-oriented grains. The orientation of the diverging GB 4 – 5 is between that of grains 4 and 5, with sidebranches emerging from both grains, i.e. close to the geometrical limit. The only notable deviation between PF and CA results is the early disappearance of grain 3 in PF results, due to early sidebranching of favorably-oriented grain 2.

Region B, at the bottom of the melt pool, contains converging (7 – 8, 8 – 9, 8 – 10, 10 – 11, 10 – 12) and diverging (9 – 10, 11 – 12) GBs. In PF simulations, sidebranching at diverging GBs and at converging GBs 8 – 9 and 10 – 11 results in early elimination of the least-favorably oriented grains 9 and 11 (considering a temperature gradient essentially vertical with a slight tilt toward the right). These grains survive longer in CA simulations. For coarse grids (bottom rows), grain 11 even survives to become one of the major grains in the final microstructure (see Fig. 2) as the temperature gradient direction tilts closer to its preferred growth direction ($\alpha \approx 45^\circ$) when the melt pool advances. Another notable difference between PF and CA is the absence in the PF map of grain 7, also victim of early sidebranching from neighboring grains.

Region C, also at the bottom of the melt pool, presents important discrepancies between the predicted maps. There, converging GBs are 15 – 16 and

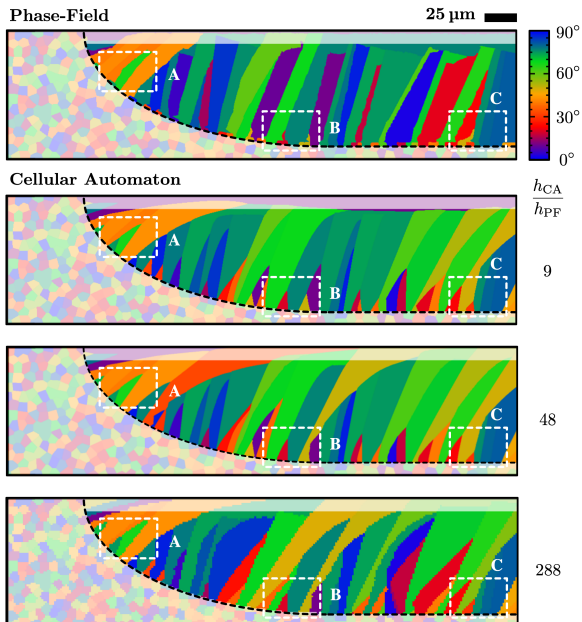


Figure 2: Selected grain orientations (color map) predicted by phase-field (top row) and cellular automaton (bottom rows) with different grid coarsening levels $h_{CA}/h_{PF} = 9, 48,$ and 288 . The brighter (washed out) area is outside of the region Γ considered for the quantitative measurements and comparisons of grain distributions. The dashed black line represents the limit of the melted region.

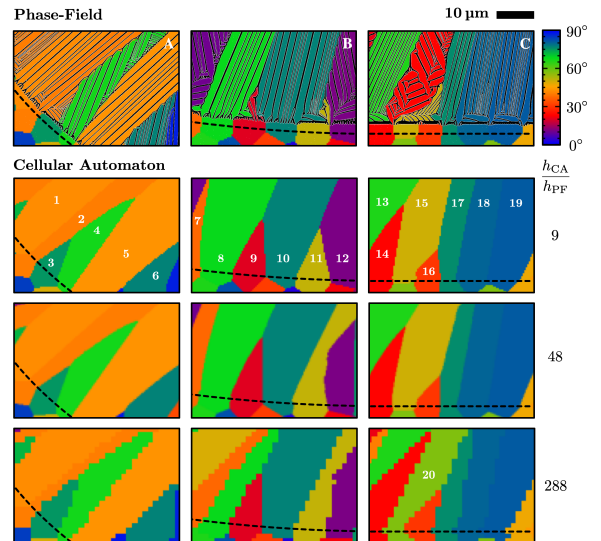


Figure 3: Comparison of selected grain orientations (color map) predicted by phase-field (top row) and cellular automaton (bottom rows) with different grid coarsening levels $h_{CA}/h_{PF} = 9, 48,$ and 288 , within the regions A, B, and C highlighted in Fig. 2. The PF grain map is overlaid with the inner grain dendritic structure. The dashed black lines show the limit of the melted region.

16 – 17, and diverging GBs are 13 – 15 and 14 – 15. Region C also contains the low-angle GBs 17 – 18 and 18 – 19. Other grain boundaries involving grain 14 (i.e. 13 – 14 and 14 – 17, the latter existing only in the PF simulation) are not clearly defined, as the misorientation with its neighbors is close to 45° . In a static temperature gradient, a misorientation of 45° with the temperature gradient would have led to the growth of a degenerate (seaweed) microstructure growing at a much higher undercooling and strongly penalized in the grain growth competition [11]. However, here, grain 14 survives for a long time in PF simulations (see Fig. 2) in spite of the strong early competition with neighbor grain 13. Here too, a major discrepancy between PF and CA stems from the early elimination of grain 15 in PF, which does not occur in CA simulation at low h_{CA} , even leading to the grain becoming one of the major grains in the subsequent grain growth competition (see Fig. 2). The coarsest CA simulation (bottom row) even leads to a completely different outcome for grain 15. The initial GB between grains 15 and 20 being close to the fusion line (black dashed line), a coarse discretization with $h_{CA}/h_{PF} \geq 288$ leads to the complete melting of grain 15, hence suppressed and replaced by lower grain 20. It follows that, as the spatial discretization gets coarser, the identity and orientation of initially competing grains may be completely changed.

A notable difference between PF and CA simulations is the presence of a region just above the fusion line that, in PF simulations, initially grows with a planar solid-liquid interface before the morphological destabilization into dendrites, after which the actual growth competition among dendrites starts. Meanwhile, in CA simulations the grains start competing from the very onset of the simulation, and the main orientation of GBs (mostly linear at this scale) is initiated directly from the fusion line. These differences between CA and PF, also observed in all cross-section simulations presented later, highlight the fact that morphological transitions (e.g. planar to dendrite) and the prediction of non-planar (rough) GBs requires the level of accuracy provided by PF.

3.3. Cross-sections

3.3.1. Effect of CA grid

Figure 4 shows the difference between CA and PF grain maps in the measured areas of the cross-section simulations for different CA grid sizes: (a) averaged over all 15 simulations or (b) averaged over the five simulations for each melt pool shape. In these cases, the primary and secondary dendrite arms spacings did not show any significant dependence on the melt pool shape, except for the wide and shallow melt pools that essentially exhibited only primary dendrites with very few secondary branches. Hence, we averaged

the spacings over all measurable simulations, yielding $\lambda_1 = 1.22 \mu\text{m}$ and $\lambda_2 = 0.82 \mu\text{m}$

While the errors at low h_{CA} , between 30% and 40%, appear slightly lower than in the longitudinal simulation, the observed trends are essentially similar. Namely, the difference between PF and CA maps increases when h_{CA} increases, and the low- h_{CA} plateau is reached at a grid size much smaller than the characteristic microstructural length scales λ_1 and λ_2 . In spite of this apparent poor PF-CA match, we show in the following subsection that, even though the discrepancy remains high when integrating the difference point-by-point, from a statistical point of view, disregarding the exact location or shape of grains, the finer CA simulations provide a good representation of the average statistical distribution of grain orientations.

3.3.2. Effect of melt pool shape

Figure 5 shows the histograms of grain distributions averaged over five simulations for the three different melt pool shapes (rows), comparing PF simulation results (lighter color) with CA predictions (darker color) with fine ($h_{CA}/h_{PF} = 3$, left) and coarse ($h_{CA}/h_{PF} = 144$, right) grids.

Simple geometrical considerations [63] suggest that, due to the main temperature gradient direction, a tran-

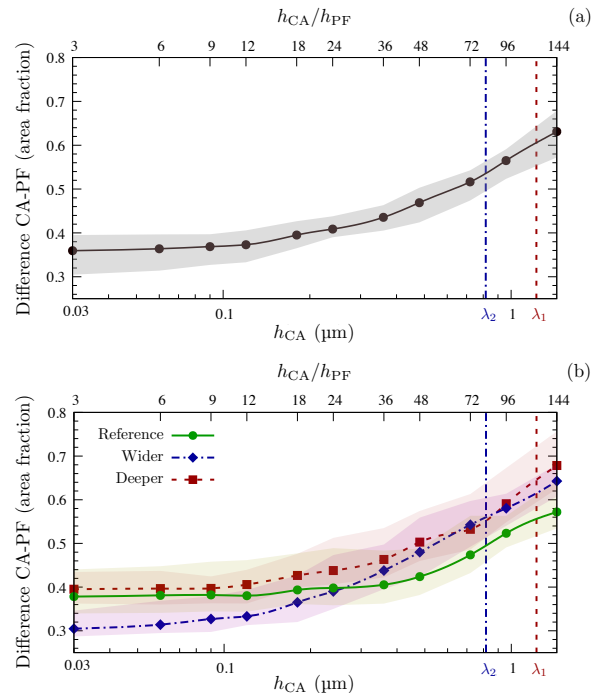


Figure 4: Difference between orientation maps in CA and PF results, as a fraction area of the measured area Γ , considering CA results in the cross-section simulations: (a) averaged over all 15 simulations, (b) averaged over five simulations for each melt pool shape (reference, wider/shallower, and deeper/narrower). The shaded area associated with each curve represents the distribution between the five different runs (minimum and maximum of CA-PF difference).

sition occurs between a predominant $\langle 100 \rangle$ grain texture in the horizontal build direction (i.e., in 2D, a high density of grains with $\alpha \approx 0^\circ$) for a relatively wide/shallow or a deep/narrow melt pool to a predominant $\langle 110 \rangle$ texture (i.e. $\alpha \approx 45^\circ$) for melt pool cross-section aspect ratio closer to unity (i.e. close to circular in shape). This trend was supported by experimental observations, for instance from powder-bed laser melting of pure copper [63] and pure molybdenum [64]. While the total number of simulations, and hence grains, presented here is not statistically sufficient to capture such a transition of grain texture, Fig. 5 exhibits clear trends in this direction, considering PF results as the most accurate ones. In particular, the wide and shallow melt pools (central row) markedly exhibit a low density of $\langle 11 \rangle$ ($\alpha \approx 45^\circ$) oriented grains and hence a stronger $\langle 10 \rangle$ ($\alpha \approx 0^\circ$) texture compared to reference (top row) and deeper/narrower (bottom row) melt pools.

For the reference melt pool shape (Fig. 5, top row), which has the aspect ratio closest to unity ($w_0/d_0 = 1.33$), the agreement between PF and CA is overall excellent, regardless of the CA grid size. Figure 6 shows the typical grain distribution in such a melt pool. In

this simulation, the selected grain orientation clearly follows the main temperature gradient direction across the melt pool. This results in a $\langle 10 \rangle$ texture (expressed with respect to the build direction, here vertical) on the sides and center of the melt pool, with intermediate orientations smoothly changing along the width of the melt pool. This trend is well captured by both CA simulations. Overall, the key differences between PF and CA simulations are: (1) the presence of the early planar growth region just above the fusion line in PF simulation, (2) the early elimination of least favorably oriented grains in PF appearing more progressively in CA simulations (as described in Section 3.2), and (3) the markedly higher roughness of grain boundaries in the PF simulations, while all GBs from CA simulations are essentially straight lines. The simulation illustrated in Fig. 6 and this characteristic distribution of grain orientations within the melt pool is representative of the trend observed in all five simulations (see all of them in Supplementary Material – Fig. B.1).

In the wider (i.e. shallower) melt pool (Fig. 5, central row), with an aspect $w_0/d_0 = 5.33$, the agreement between PF and CA is excellent for fine CA grids (left column), but a notable discrepancy appears for coarser CA grids (right column). Figure 7 illustrates the selected grain maps for a given initial grain distribution,

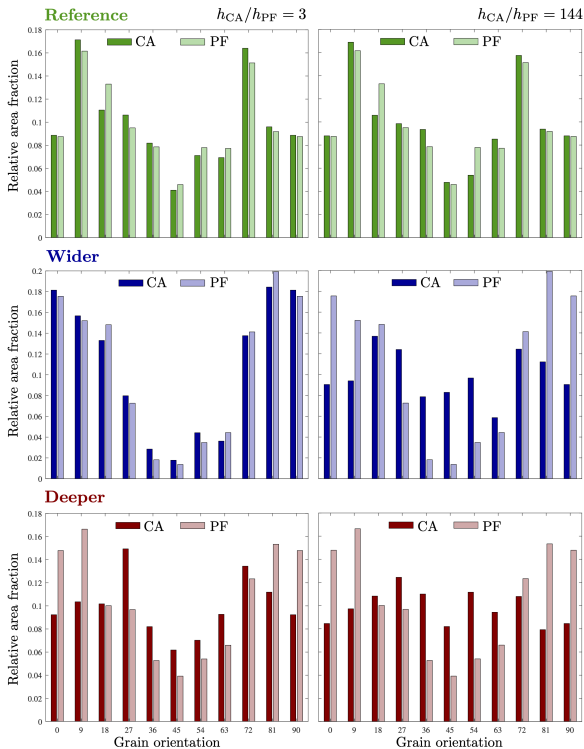


Figure 5: Distribution of grain orientations, averaged over five simulations for three different melt pool shapes, namely the reference case fitted to FE results (top row), a wider and shallower melt pool (central row), and a deeper and narrower melt pool (bottom row), comparing PF and CA results for a fine ($h_{CA}/h_{PF} = 3$, left column) and a coarse ($h_{CA}/h_{PF} = 144$, right column) CA grid. (PF results are the same in left and right columns, only duplicated for readability.)

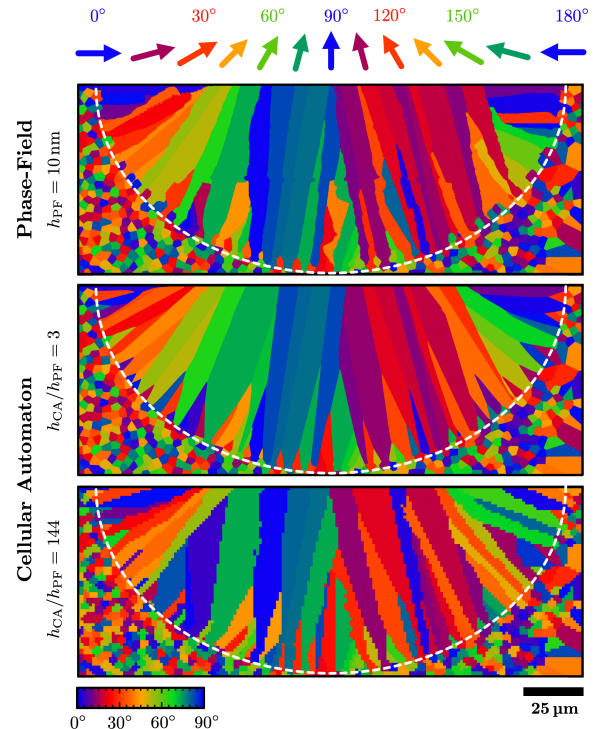


Figure 6: Grain orientation maps for the reference melt pool dimension given by FE thermal simulation ($w_0 = 128 \mu\text{m}$, $d_0 = 96 \mu\text{m}$), predicted by phase field (top row) compared to CA with fine (central row) and coarse (bottom row) grid. The white dashed lines identify the melted region. Arrows at the top illustrate the predominant selected grain orientations within the melt pool.

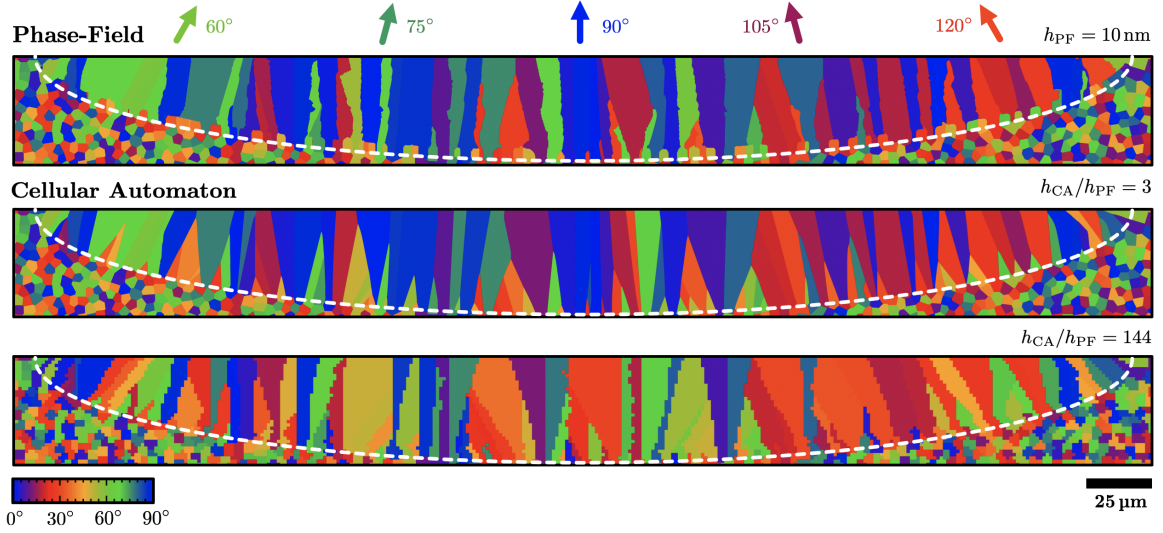


Figure 7: Grain orientation maps for a wide and shallow melt pool ($w_0 = 256 \mu\text{m}$, $d_0 = 48 \mu\text{m}$), predicted by phase field (top row) compared to CA with fine (central row) and coarse (bottom row) grid. The white dashed lines identify the melted region. Arrows at the top illustrate the predominant selected grain orientations within the melt pool.

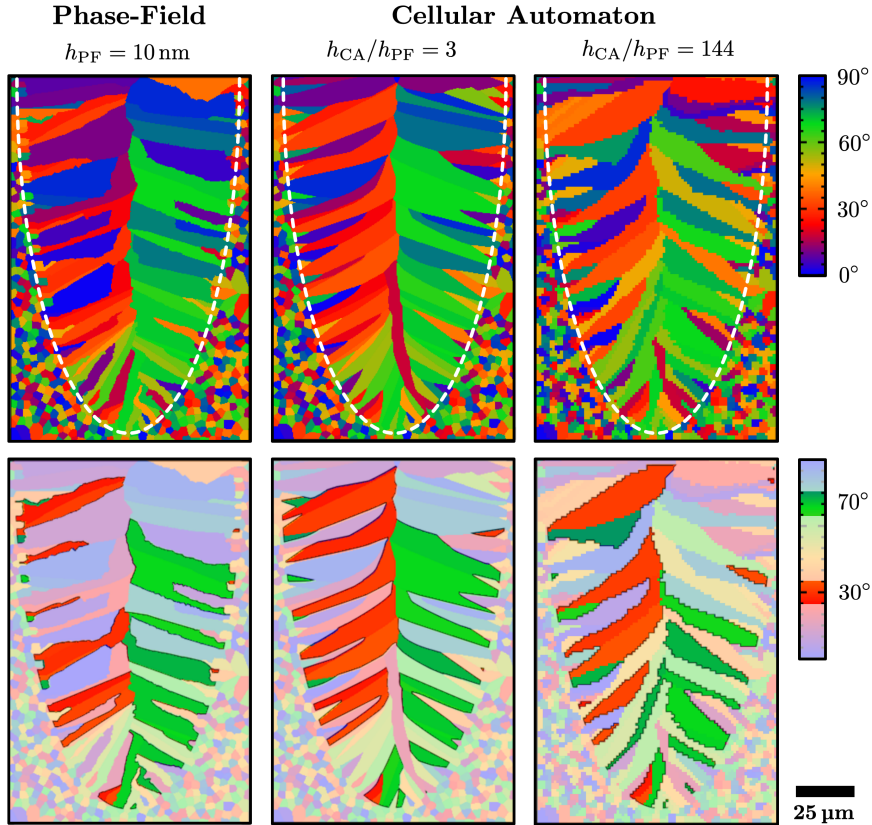


Figure 8: Grain orientation maps for a deep and narrow melt pool ($w_0 = 64 \mu\text{m}$, $d_0 = 192 \mu\text{m}$), predicted by phase field (left column) compared to CA with fine (central column) and coarse (right column) grid. The white dashed lines identify the melted region. The bottom row highlights grains with orientations $25^\circ \leq \alpha \leq 35^\circ$ (red) and $65^\circ \leq \alpha \leq 75^\circ$ (green).

representative of the behavior observed in all five configurations (see all of them Supplementary Material – Fig. B.2) In this case, the temperature gradient is essentially oriented upwards. Therefore, it is not surprising to observe that in the PF simulations, the vast ma-

jority of selected grains have their orientation within $\alpha = 90^\circ \pm 30^\circ$. For a coarser CA grid (bottom row), the distribution of grain orientations across the melt pool is more scattered, and several grain with $\alpha \approx 45^\circ$ even appear within the solidified melt pool. Similarly as in

previously described cases, the initial planar growth followed by early elimination of unfavorably oriented grains (resulting in little square grains just above the fusion line) is observed only in PF simulations, which also exhibits notably rougher GBs.

For the deeper (i.e. narrower) melt pools (Fig. 5, bottom row), the agreement between CA and PF grain orientation densities is notably worse, and it only marginally improves with lower h_{CA} . However, in spite of a relatively higher discrepancy in their relative amount, Figure 8 shows that both PF and CA qualitatively match reasonably well in terms of texture distribution within the melt pool, commensurately with the main temperature gradient direction therein. The left-hand side of the melt pool is mostly composed of grains with orientation $0^\circ \leq \alpha \leq 35^\circ$, while the right-hand side exhibits a high density of grain with $55^\circ \leq \alpha \leq 90^\circ$. This left-right segregation of grain orientations is highlighted in the bottom part of Fig. 8, where orientations are highlighted that fall between 25° and 35° (red) and between 65° and 75° (green). Compared to the reference and wide melt pool cases, in which CA-predicted GBs are essentially straight lines, those in the deeper melt pool are more curved, as they follow the rotation of the main temperature gradient direction during the melt pool solidification. In the PF simulation, this overall rotation of the grain from horizontal to upwards also appears, but the morphologies of GBs are, once again, rougher than in CA simulations. This behavior is representative of observations in all five simulated deep melt pools (see Supplementary Material – Fig. B.3).

4. Summary, Conclusions, and Perspectives

In this article, we performed systematic comparisons between grain microstructures selected during the polycrystalline solidification of a melt pool predicted by phase-field and cellular automaton techniques. We used a binary Ni-5wt%Nb as model alloy, and a thermal field calculated by finite elements thermal simulations for an Inconel 718 alloy [42], and analyzed 2D simulations of solidification in the longitudinal direction [42], as well as different melt pool shapes in the cross-section normal to the scanning direction.

Our simulations revealed that the exact matching of grain structures, i.e. comparing detailed grain and GB morphologies, essentially improves with the refinement of the CA grid. When comparing/integrating grain orientation maps point-by-point, the best CA simulations capture the PF grain maps over only 70% of the melted region at best. However, while specific details at the scale of individual grains and GBs are not accurately reproduced, the overall statistical distribution of crystal orientations in the entire melt pools, averaged over several runs, is relatively well predicted by CA

simulations using finer grids, for a fraction of the PF computational cost. This agreement seems to depend also on the melt pool shape, as we found poorer matching for the deeper melt pools – which we attribute to the stronger change in temperature profile and gradient directions during solidification.

Looking at the detailed GB scale, the trajectories of converging and low angle GBs are most often (yet not always) well captured, as most of them tend to follow the classical favorably-oriented grain criterion. The discrepancy is higher for high-angle diverging GBs.

Some striking differences appear between PF and CA related to transient growth regime and solid-liquid interface morphology. Indeed, PF simulations systematically lead to an initial transient solidification period with a nearly planar solid-liquid interface, until its velocity increases enough to lead to a morphological destabilization into cells or dendrites. This is not captured by CA simulations, in which the grains start competing directly from the onset of the simulation (i.e. from the fusion line). In PF simulations, the transient destabilization of the planar interface into dendrites also gives rise to intense sidebranching activity, from which the least favorably oriented grains (i.e. those with higher misorientation of their preferred growth direction with the temperature gradient) are often rapidly eliminated by favorably oriented neighbors. This dynamics of sidebranching following the morphological destabilization of the interface is not captured by CA simulations. Moreover, the CA-predicted GBs are much smoother than the rough ones emerging from PF simulations.

Regarding the effect of the melt pool shape, melt pools with an aspect ratio close to unity (i.e. near circular) exhibit a good agreement between CA and PF statistical distribution of grain orientations, as well as their distribution within the melt pool. The CA-PF agreement becomes lower, and more grid-dependent, for higher aspect ratio of the melt pool, while the overall distribution of grain orientations across the melt pool remains reasonable. Our 15 configurations did not provide enough statistics to unambiguously capture the transition from $\langle 100 \rangle$ to $\langle 110 \rangle$ as a function of melt pool aspect ratio [63]. However, PF, and to some extent fine-grid CA simulations, show clear indications that such experimentally-observed transition [63, 64] can be predicted, should the number of simulations (and hence grains) be increased to a more statistically significant amount.

Furthermore, our simulations did not exhibit a strong dependence upon the considered CA neighborhood algorithm (Moore or von Neumann) nor upon the dendrite growth kinetics law $V(\Delta T)$ applied at the grain vertices. We attribute the latter to the high temperature gradient, reducing the distance between solidus and liquidus isotherms, and hence reducing the effect of the growth law upon the location of the solid-

ification front between T_L and T_S .

Some limitations of the current study are worth highlighting, several of which are actually the focus of ongoing work building up from this study. First, solidification simulations presented here, while based on 3D calculation of the temperature field, are two-dimensional, thus not capturing the full complexity of grain growth competition in an actual melt pool. However, the present study would, at present, not be possible in 3D, as the grid size required by well-converged PF simulations already leads to sizable 2D simulations, handled here with an advanced multi-GPU parallelized implementation. Other important phenomena present during melt pool solidification were ignored, such as fluid flow and nucleation. The latter would specifically deserve a closer look, as nucleation parameters (e.g. undercooling and site density) are almost systematically taken as calibration parameters in both PF and CA simulations. Finally, more advanced CA formulations, e.g. using irregular quadrangles instead of square building blocks [61, 68, 69], could also have a key influence, considering the high temperature gradients encountered in AM-relevant conditions.

In spite of these limitations, we trust that the presented results bring some useful insight into the applicability and limitations of both modeling methods. They clearly show that, when considering microstructural details at the scale of individual grains or GBs, the accuracy of PF remains required to capture transient growth kinetics and solid-liquid interface morphological evolution. The prediction of transient growth regimes in CA simulations might be improved using more advanced growth kinetics [69] instead of the classical Ivantsov- or KGT-based ones. However, the modeling of the morphological stability of a solid-liquid interface unambiguously requires the level of details provided only by PF. This is even more important in AM-relevant conditions, that may lead to the restabilization of a planar interface at high growth velocity, called *absolute stability* [70, 71], and evidenced in several rapidly solidified alloys in the form of banded microstructures [72–74]. Still, when the most important length scale is that of the average grain microstructure, e.g. to predict averaged anisotropic mechanical properties over representative volume elements [75], our results show that CA-based methods are capable of statistically reasonable grain texture predictions. As similar quantitative PF simulations in 3D are currently computationally out of reach, the substantial speed-up and upscaling afforded by CA modeling provides a most promising route for the prediction of actual three-dimensional AM microstructures.

Acknowledgements

This work was supported by the Spanish Ministry of Science and the European Union NextGenerationEU

(PRTR) through the MiMMoSA project [PCI2021-122023-2B] and a Ramón y Cajal fellowship [RYC2019-028233-I].

References

- [1] B. E. Carroll, T. A. Palmer, A. M. Beese, Anisotropic tensile behavior of ti-6al-4v components fabricated with directed energy deposition additive manufacturing, *Acta Materialia* 87 (2015) 309–320.
- [2] M. M. Kirka, F. Medina, R. Dehoff, A. Okello, Mechanical behavior of post-processed inconel 718 manufactured through the electron beam melting process, *Materials Science and Engineering: A* 680 (2017) 338–346.
- [3] J. Gordon, C. Haden, H. Nied, R. Vinci, D. Harlow, Fatigue crack growth anisotropy, texture and residual stress in austenitic steel made by wire and arc additive manufacturing, *Materials Science and Engineering: A* 724 (2018) 431–438.
- [4] B. Mooney, K. I. Kourousis, R. Raghavendra, D. Agius, Process phenomena influencing the tensile and anisotropic characteristics of additively manufactured maraging steel, *Materials Science and Engineering: A* 745 (2019) 115–125.
- [5] E. Hosseini, V. Popovich, A review of mechanical properties of additively manufactured inconel 718, *Additive Manufacturing* 30 (2019) 100877.
- [6] D. Walton, B. Chalmers, The origin of the preferred orientation in the columnar zone of ingots, *Trans, AIME* 215 (1959) 447–456.
- [7] N. D’souza, M. Ardakani, A. Wagner, B. Shollock, M. McLean, Morphological aspects of competitive grain growth during directional solidification of a nickel-base superalloy, *cmsx4*, *Journal of materials science* 37 (3) (2002) 481–487.
- [8] A. Wagner, B. Shollock, M. McLean, Grain structure development in directional solidification of nickel-base superalloys, *Materials Science and Engineering: A* 374 (1-2) (2004) 270–279.
- [9] Y. Zhou, A. Volek, N. Green, Mechanism of competitive grain growth in directional solidification of a nickel-base superalloy, *Acta Materialia* 56 (11) (2008) 2631–2637.
- [10] J. Li, Z. Wang, Y. Wang, J. Wang, Phase-field study of competitive dendritic growth of converging grains during directional solidification, *Acta Materialia* 60 (4) (2012) 1478–1493.
- [11] D. Tourret, A. Karma, Growth competition of columnar dendritic grains: A phase-field study, *Acta Materialia* 82 (2015) 64–83.
- [12] T. Takaki, M. Ohno, Y. Shibuta, S. Sakane, T. Shimokawabe, T. Aoki, Two-dimensional phase-field study of competitive grain growth during directional solidification of polycrystalline binary alloy, *Journal of Crystal Growth* 442 (2016) 14–24.
- [13] D. Tourret, Y. Song, A. J. Clarke, A. Karma, Grain growth competition during thin-sample directional solidification of dendritic microstructures: A phase-field study, *Acta Materialia* 122 (2017) 220–235.
- [14] F. Mota, N. Bergeon, D. Tourret, A. Karma, R. Trivedi, B. Billia, Initial transient behavior in directional solidification of a bulk transparent model alloy in a cylinder, *Acta Materialia* 85 (2015) 362–377.
- [15] Y. Song, D. Tourret, F. Mota, J. Pereda, B. Billia, N. Bergeon, R. Trivedi, A. Karma, Thermal-field effects on interface dynamics and microstructure selection during alloy directional solidification, *Acta Materialia* 150 (2018) 139–152.
- [16] F. Mota, J. Pereda, K. Ji, Y. Song, R. Trivedi, A. Karma, N. Bergeon, Effect of sub-boundaries on primary spacing dynamics during 3d directional solidification conducted on declic-dsi, *Acta Materialia* 204 (2021) 116500.

- [17] Z. Liu, M. Lin, D. Yu, X. Zhou, Y. Gu, H. Fu, Dependence of competitive grain growth on secondary dendrite orientation during directional solidification of a ni-based superalloy, *Metallurgical and Materials Transactions A* 44 (11) (2013) 5113–5121.
- [18] H. Yu, J. Li, X. Lin, L. Wang, W. Huang, Anomalous overgrowth of converging dendrites during directional solidification, *Journal of crystal growth* 402 (2014) 210–214.
- [19] S. Hu, L. Liu, W. Yang, J. Zhang, T. Huang, Y. Wang, X. Zhou, Competitive converging dendrites growth depended on dendrite spacing distribution of ni-based bicrystal superalloys, *Journal of Alloys and Compounds* 735 (2018) 1878–1884.
- [20] Y. Wang, S. Li, Z. Liu, B. Yang, H. Zhong, H. Xing, Competitive growth of degenerate pattern and dendrites during directional solidification of a bicrystal metallic alloy, *Metallurgical and Materials Transactions A* 50 (10) (2019) 4677–4685.
- [21] P. Zhao, J. Heinrich, Front-tracking finite element method for dendritic solidification, *Journal of Computational Physics* 173 (2) (2001) 765–796.
- [22] C.-Y. Li, S. V. Garimella, J. E. Simpson, Fixed-grid front-tracking algorithm for solidification problems, part i: Method and validation, *Numerical Heat Transfer, Part B: Fundamentals* 43 (2) (2003) 117–141.
- [23] T. M. Rodgers, J. D. Madison, V. Tikare, Simulation of metal additive manufacturing microstructures using kinetic monte carlo, *Computational Materials Science* 135 (2017) 78–89.
- [24] T. M. Rodgers, D. Moser, F. Abdeljawad, O. D. U. Jackson, J. D. Carroll, B. H. Jared, D. S. Bolintineanu, J. A. Mitchell, J. D. Madison, Simulation of powder bed metal additive manufacturing microstructures with coupled finite difference-monte carlo method, *Additive Manufacturing* 41 (2021) 101953.
- [25] P. Jreidini, T. Pinomaa, J. M. Wiezorek, J. T. McKeown, A. Laukkanen, N. Provatas, Orientation gradients in rapidly solidified pure aluminum thin films: comparison of experiments and phase-field crystal simulations, *Physical review letters* 127 (20) (2021) 205701.
- [26] Y.-T. Kim, N. Goldenfeld, J. Dantzig, Computation of dendritic microstructures using a level set method, *Physical Review E* 62 (2) (2000) 2471.
- [27] F. Gibou, R. Fedkiw, R. Caflisch, S. Osher, A level set approach for the numerical simulation of dendritic growth, *Journal of Scientific Computing* 19 (1) (2003) 183–199.
- [28] I. Steinbach, C. Beckermann, B. Kauerauf, Q. Li, J. Guo, Three-dimensional modeling of equiaxed dendritic growth on a mesoscopic scale, *Acta Materialia* 47 (3) (1999) 971–982.
- [29] Y. Souhar, V. F. De Felice, C. Beckermann, H. Combeau, M. Založnik, Three-dimensional mesoscopic modeling of equiaxed dendritic solidification of a binary alloy, *Computational Materials Science* 112 (2016) 304–317.
- [30] A. Viardin, M. Založnik, Y. Souhar, M. Apel, H. Combeau, Mesoscopic modeling of spacing and grain selection in columnar dendritic solidification: Envelope versus phase-field model, *Acta Materialia* 122 (2017) 386–399.
- [31] D. Tourret, A. Karma, Three-dimensional dendritic needle network model for alloy solidification, *Acta Materialia* 120 (2016) 240–254.
- [32] T. Isensee, D. Tourret, Convective effects on columnar dendritic solidification—a multiscale dendritic needle network study, *Acta Materialia* (2022) 118035.
- [33] M. Rappaz, C.-A. Gandin, Probabilistic modelling of microstructure formation in solidification processes, *Acta metallurgica et materialia* 41 (2) (1993) 345–360.
- [34] C.-A. Gandin, M. Rappaz, A coupled finite element-cellular automaton model for the prediction of dendritic grain structures in solidification processes, *Acta metallurgica et materialia* 42 (7) (1994) 2233–2246.
- [35] W. J. Boettinger, J. A. Warren, C. Beckermann, A. Karma, Phase-field simulation of solidification, *Annual review of materials research* 32 (1) (2002) 163–194.
- [36] D. Tourret, H. Liu, J. Llorca, Phase-field modeling of microstructure evolution: Recent applications, perspectives and challenges, *Progress in Materials Science* 123 (2022) 100810.
- [37] I. Steinbach, Phase-field models in materials science, *Modelling and simulation in materials science and engineering* 17 (7) (2009) 073001.
- [38] A. Karma, W. Rappel, Quantitative phase-field modeling of dendritic growth in two and three dimensions, *Physical Review E* 57 (4) (1998) 4323.
- [39] B. Echebarria, R. Folch, A. Karma, M. Plapp, Quantitative phase-field model of alloy solidification, *Physical review E* 70 (6) (2004) 061604.
- [40] Y. Shibuta, M. Ohno, T. Takaki, Solidification in a supercomputer: from crystal nuclei to dendrite assemblages, *Jom* 67 (8) (2015) 1793–1804.
- [41] T. Shimokawabe, T. Aoki, T. Takaki, T. Endo, A. Yamanaka, N. Maruyama, A. Nukada, S. Matsuoka, Peta-scale phase-field simulation for dendritic solidification on the tsubame 2.0 supercomputer, in: *Proceedings of 2011 International Conference for High Performance Computing, Networking, Storage and Analysis*, 2011, pp. 1–11.
- [42] S. Elahi, R. Tavakoli, A. Boukellal, T. Isensee, I. Romero, D. Tourret, Multiscale simulation of powder-bed fusion processing of metallic alloys, *Computational Materials Science* 209 (2022) 111383.
- [43] S. Chen, G. Guillemot, C.-A. Gandin, Three-dimensional cellular automaton-finite element modeling of solidification grain structures for arc-welding processes, *Acta materialia* 115 (2016) 448–467.
- [44] A. Rai, M. Markl, C. Körner, A coupled cellular automaton–lattice boltzmann model for grain structure simulation during additive manufacturing, *Computational Materials Science* 124 (2016) 37–48.
- [45] J. Koepf, D. Soldner, M. Ramsperger, J. Mergheim, M. Markl, C. Körner, Numerical microstructure prediction by a coupled finite element cellular automaton model for selective electron beam melting, *Computational Materials Science* 162 (2019) 148–155.
- [46] Y. Lian, Z. Gan, C. Yu, D. Kats, W. K. Liu, G. J. Wagner, A cellular automaton finite volume method for microstructure evolution during additive manufacturing, *Materials & Design* 169 (2019) 107672.
- [47] M. S. Mohebbi, V. Ploshikhin, Implementation of nucleation in cellular automaton simulation of microstructural evolution during additive manufacturing of al alloys, *Additive Manufacturing* 36 (2020) 101726.
- [48] K. Teferra, D. J. Rowenhorst, Optimizing the cellular automata finite element model for additive manufacturing to simulate large microstructures, *Acta Materialia* 213 (2021) 116930.
- [49] G. IVANTSOV, Temperature field around a spherical cylindrical and a circular crystal growing in a supercooled melt, in: *Dokl. Akad. Nauk SSSR*, Vol. 58, 1947, pp. 567–569.
- [50] W. Kurz, B. Giovanola, R. Trivedi, Theory of microstructural development during rapid solidification, *Acta metallurgica* 34 (5) (1986) 823–830.
- [51] T. Carozzani, H. Dignonnet, C.-A. Gandin, 3d cafe modeling of grain structures: application to primary dendritic and secondary eutectic solidification, *Modelling and Simulation in Materials Science and Engineering* 20 (1) (2011) 015010.
- [52] W. Wang, P. D. Lee, M. Mclean, A model of solidification microstructures in nickel-based superalloys: predicting primary dendrite spacing selection, *Acta materialia* 51 (10) (2003) 2971–2987.
- [53] H. Yin, S. Felicelli, L. Wang, Simulation of a dendritic microstructure with the lattice boltzmann and cellular automaton methods, *Acta Materialia* 59 (8) (2011) 3124–3136.
- [54] A. Choudhury, K. Reuther, E. Wesner, A. August, B. Nestler, M. Rettenmayr, Comparison of phase-field and

- cellular automaton models for dendritic solidification in al-cu alloy, *Computational Materials Science* 55 (2012) 263–268.
- [55] M. Eshraghi, B. Jelinek, S. D. Felicelli, Large-scale three-dimensional simulation of dendritic solidification using lattice boltzmann method, *Jom* 67 (8) (2015) 1786–1792.
- [56] C. A. Gandin, M. Rappaz, D. West, B. Adams, Grain texture evolution during the columnar growth of dendritic alloys, *Metallurgical and Materials Transactions A* 26 (6) (1995) 1543–1551.
- [57] M. Rappaz, C. A. Gandin, J.-L. Desbiolles, P. Thevoz, Prediction of grain structures in various solidification processes, *Metallurgical and Materials Transactions A* 27 (3) (1996) 695–705.
- [58] H. Takatani, C.-A. Gandin, M. Rappaz, Ebsd characterisation and modelling of columnar dendritic grains growing in the presence of fluid flow, *Acta materialia* 48 (3) (2000) 675–688.
- [59] P. Carter, D. Cox, C.-A. Gandin, R. C. Reed, Process modelling of grain selection during the solidification of single crystal superalloy castings, *Materials Science and Engineering: A* 280 (2) (2000) 233–246.
- [60] C.-A. Gandin, M. Rappaz, A 3d cellular automaton algorithm for the prediction of dendritic grain growth, *Acta Materialia* 45 (5) (1997) 2187–2195.
- [61] A. Pineau, G. Guillemot, D. Tourret, A. Karma, C.-A. Gandin, Growth competition between columnar dendritic grains—cellular automaton versus phase field modeling, *Acta Materialia* 155 (2018) 286–301.
- [62] E. Dorari, K. Ji, G. Guillemot, C.-A. Gandin, A. Karma, Growth competition between columnar dendritic grains—the role of microstructural length scales, *Acta Materialia* 223 (2022) 117395.
- [63] S. D. Jadhav, S. Dadbakhsh, L. Goossens, J. Kruth, J. Van Humbeeck, K. Vanmeensel, Influence of selective laser melting process parameters on texture evolution in pure copper, *Journal of Materials Processing Technology* 270 (2019) 47–58.
- [64] M. Higashi, T. Ozaki, Selective laser melting of pure molybdenum: evolution of defect and crystallographic texture with process parameters, *Materials & Design* 191 (2020) 108588.
- [65] K. Glasner, Nonlinear preconditioning for diffuse interfaces, *J Comput Phys* 174 (2) (2001) 695–711.
- [66] K. Karayagiz, L. Johnson, R. Seede, V. Attari, B. Zhang, X. Huang, S. Ghosh, T. Duong, I. Karaman, A. Elwany, et al., Finite interface dissipation phase field modeling of ni-nb under additive manufacturing conditions, *Acta Materialia* 185 (2020) 320–339.
- [67] C. Gandin, J.-L. Desbiolles, M. Rappaz, P. Thevoz, et al., A three-dimensional cellular automation-finite element model for the prediction of solidification grain structures, *Metallurgical and Materials Transactions A* 30 (12) (1999) 3153–3165.
- [68] T. Carozzani, Développement d’un modèle 3d automate cellulaire-éléments finis (cafe) parallèle pour la prédiction de structures de grains lors de la solidification d’alliages métalliques, Ph.D. thesis, Ecole Nationale Supérieure des Mines de Paris (2012).
- [69] R. Fleurisson, O. Senninger, G. Guillemot, C.-A. Gandin, Hybrid cellular automaton-parabolic thick needle model for equiaxed dendritic solidification, *Journal of Materials Science & Technology* 124 (2022) 26–40.
- [70] W. W. Mullins, R. Sekerka, Stability of a planar interface during solidification of a dilute binary alloy, *Journal of applied physics* 35 (2) (1964) 444–451.
- [71] W. Kurz, R. Trivedi, Rapid solidification processing and microstructure formation, *Materials Science and Engineering: A* 179 (1994) 46–51.
- [72] M. Carrard, M. Gremaud, M. Zimmermann, W. Kurz, About the banded structure in rapidly solidified dendritic and eutectic alloys, *Acta metallurgica et materialia* 40 (5) (1992) 983–996.
- [73] W. Kurz, R. Trivedi, Banded solidification microstructures, *Metallurgical and Materials Transactions A* 27 (3) (1996) 625–634.
- [74] J. T. McKeown, K. Zwiack, C. Liu, D. R. Coughlin, A. J. Clarke, J. K. Baldwin, J. W. Gibbs, J. D. Roehling, S. D. Imhoff, P. J. Gibbs, et al., Time-resolved in situ measurements during rapid alloy solidification: Experimental insight for additive manufacturing, *Jom* 68 (3) (2016) 985–999.
- [75] C. M. Pilgar, A. M. Fernandez, S. Lucarini, J. Segurado, Effect of printing direction and thickness on the mechanical behavior of slm fabricated hastelloy-x, *International Journal of Plasticity* 153 (2022) 103250.

Grain growth competition during melt pool solidification – Comparing phase-field and cellular automaton models

Supplementary Material

S.M. Elahi^{a,b}, R. Tavakoli^b, I. Romero^{a,b}, D. Tourret^b

^a *Universidad Politécnica de Madrid, E.T.S. de Ingenieros Industriales, Madrid, Spain.*

^b *IMDEA Materials Institute, C/ Eric Kandel 2, 28906, Getafe, Madrid, Spain.*

Contents

A	Analytical approximation of the temperature field in the melt pool region	1
B	Cross section grain maps	3
C	Computational performance	3

A. Analytical approximation of the temperature field in the melt pool region

Based on the finite elements (FE) simulations of laser melting of Inconel 718 alloy performed in Ref. [1], we approximate the temperature field in the melt pool region along longitudinal and cross-section using analytical functions. These functions represent the location of liquidus (T_L) and solidus (T_S) isotherms as ellipsis. The function used along the longitudinal section is presented and discussed in details in Ref. [1]. The function used along the cross section (schematized in Fig. A.1) is given by:

$$T(r, \theta) = T_0(\theta, t) + (T_S - T_0(\theta, t)) \frac{r}{r_S(\theta, t)} \quad (\text{A.1})$$

$$r_S(\theta) = \sqrt{\frac{(w_S(t)d_S(t))^2}{(d_S(t) \cos(\theta))^2 + (w_S(t) \sin(\theta))^2}} \quad (\text{A.2})$$

with

$$r = \sqrt{(x - x_0)^2 + (y - y_0)^2} \quad (\text{A.3})$$

$$\theta = \tan^{-1} \left| \frac{y - y_0}{x - x_0} \right| \quad (\text{A.4})$$

and

$$w_S(t) = w_0 \times [1 - (t/t_f)^{n_w}] \quad (\text{A.5})$$

$$d_S(t) = d_0 \times [1 - (t/t_f)^{n_d}] \quad (\text{A.6})$$

$$T_0(\theta, t) = \frac{T_1(\theta) + T_2(t)}{2} - \frac{T_1(\theta) - T_2(t)}{2} \times \tanh\left(\frac{t - \tau(\theta)}{\sigma(\theta)}\right) \quad (\text{A.7})$$

$$T_1(\theta) = T_w - (T_w - T_d) \times \sin(\theta) \quad (\text{A.8})$$

$$T_2(t) = T_L - R \times (t - t_L) \quad (\text{A.9})$$

$$\tau(\theta) = \tau_w - (\tau_w - \tau_d) \times \sin(\theta) \quad (\text{A.10})$$

$$\sigma(\theta) = \sigma_w - (\sigma_w - \sigma_d) \times \sin(\theta) \quad (\text{A.11})$$

$$(\text{A.12})$$

Here, $w_S(t)$ and $d_S(t)$ represent, respectively, the half-width and depth of the solidus temperature (T_S) location, while $T_0(\theta, t)$ extrapolates the temperature at the center of the melt pool, i.e. at $(x, y) = (0, 0)$. The melt pool center temperature $T_0(\theta, t)$ transitions from an early stage $T_1(\theta)$ to a later stage $T_2(t)$ using a sigmoid function (Eq. (A.7)). $T_1(\theta)$ is extrapolated from liquidus and solidus temperature locations along the width (T_w) and depth (T_d) of the melt pool. $T_2(t)$ is fitted to the late stage ($T_0 < T_L$) temperature evolution of the temperature. Function $T_1(\theta)$ and the sigmoid transition time and duration (parametrized using $\tau(\theta)$ and $\sigma(\theta)$) are interpolated between the melt pool width ($\theta = 0$) and depth ($\theta = \pi/2$) directions using sine functions (Eqs (A.8), (A.10) and (A.11)).

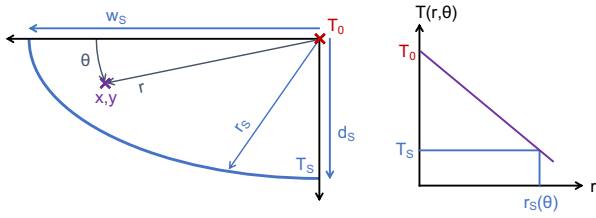


Figure A.1: Schematics of analytical temperature approximation $T(r, \theta)$: (left) location of elliptical solidus isotherm from the center (x_0, y_0) of the melt pool, (right) radial interpolation between center temperature T_0 and solidus temperature T_s .

Hence, values of T_w , T_d , τ_w , τ_d , σ_w , and σ_d are adjusted to fit the time evolution of the width and depth of the solidus (T_s) and liquidus (T_L) temperatures (Fig. A.2a), while R is adjusted to match the cooling rate of T_0 once it falls below T_L (Fig. A.2b), which can all be adjusted to match an arbitrary temperature profile, e.g. that calculated with FE in Ref. [1].

While arguably approximate, this analytical function has several advantages: (1) it allows a reasonable description of the time evolution of both solidus (T_s) and liquidus (T_L) width and depth, with an elliptical interpolation for $0 < \theta < \pi/2$ and a linear (radial) interpolation between T_s and T_L (where most of the solidification takes place); (2) it smoothly and continuously interpolates in time between T_1 and T_2 when $T_0 \approx T_L$, as long as appropriate values are chosen for τ_w , τ_d , σ_w , and σ_d for this transition to occur early enough; and (3) it allows avoiding infinite temperature gradient at the melt pool center when T_0 gets close to T_s , possible with simpler function (e.g. of the form used in the longitudinal section), as long as the late-stage cooling rate R is high enough.

Figures below illustrate the equations above adjusted to the published FE results using $t_L = 0.00195$ s, $t_f = 0.00255$ s, $w_0 = 128$ μm , $d_0 = 96$ μm , $n_w = 20$, $n_d = 3$, $T_w = 2700$ K, $T_d = 2450$ K, $\tau_w = 0.00115$ s, $\tau_d = 0.0007$ s, $\sigma_w = 0.00036$ s, $\sigma_d = 0.0005$ s, and $R = 1.2 \times 10^5$ K/s, considering $T_L = 1625$ K and $T_s = 1554$ K. While the peculiar shape of the solidus isotherm – namely the cusps due to the lower thermal conductivity of the powder bed on the sides compared to the high conductivity of the dense solidified metal at the bottom [1] – cannot be accurately modeled using elliptical isotherms, the figure shows that the time evolution of the solidus and liquidus isotherms is reasonably approximated by the chosen function.

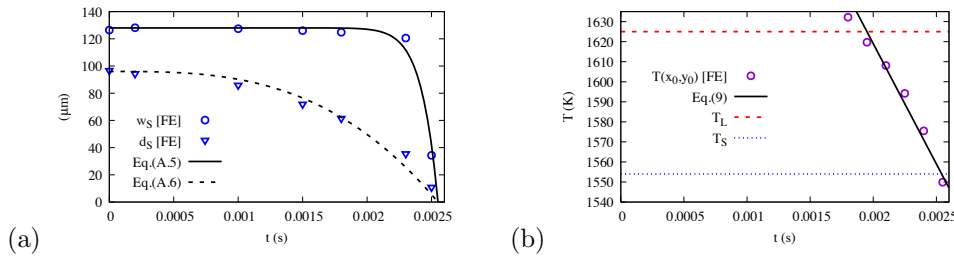


Figure A.2: (a) Time evolution of solidus isotherm half-width (w_s) and depth d_s comparing FE results (symbols) and Eqs. (A.5)-(A.5) (lines). (b) Time evolution of the temperature at the center of the melt pool T_0 between T_L and T_s , comparing FE results (symbols) with Eq. (A.9) (solid line).

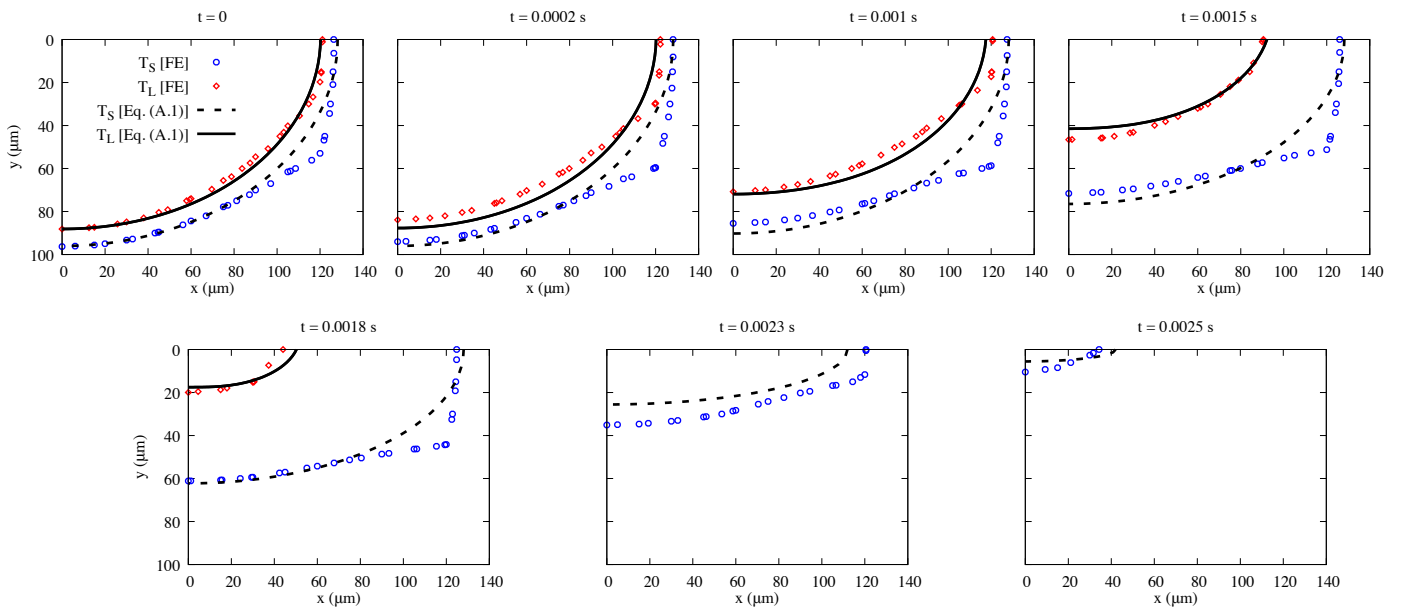


Figure A.3: Time evolution (snapshots) of the locations of the solidus and liquidus isotherms in a cross section, comparing FE results of Ref. [1] (symbols) to Eq. (A.1) (lines).

B. Cross section grain maps

See next pages.

C. Computational performance

Tables below summarize the computational performance of the various simulations in terms of simulation (wall) time and speed-up (wall time ratio) from cellular automaton (CA) compared to phase-field (PF) simulations. Note that we are comparing PF simulations performed on multiple GPUs (each with thousands of CUDA cores) to CA simulations performed on a single core on a desktop or laptop computer. For a similar simulation, the speed-up from a single core to a single-GPU parallel implementation is roughly of order $20\times$ and the strong scaling with the number of GPUs (here 2 to 8) was also observed to be nearly linear – both effects advantaging the PF performance by a significant amount in the tables below. Also note the significant differences in computing time when using different GPU models, e.g. with a factor of $\approx 1.4\times$ between the cross-section reference PF calculations, performed on two RTX3090 (faster) and the wide/shallow PF simulations performed on two RTX2080Ti (slower), while the simulation size is nearly identical.

Method:	Phase-Field		Cellular Automaton	
Hardware:	$8 \times$ RTX2080Ti	$1 \times$ Intel Xeon 6130 core (2.10 GHz)		
	Wall time	h_{CA}/h_{PF}	Wall time	Speed-up PF/CA
	9d16h (232h)	6	10d10h	0.93
		12	1d08h	7.2
		24	4h02m	58
		48	32m	430
		96	4m	3 500
		192	33s	25 000
		384	4s	210 000
		768	1s	840 000

Table C.1: Computational performance for **longitudinal section** simulations.

Method:	Phase-Field		Cellular Automaton	
Hardware:	$2 \times$ RTX3090	$1 \times$ Intel Xeon 6130 core (2.10 GHz)		
	Wall time	h_{CA}/h_{PF}	Wall time	Speed-up PF/CA
	1d19h (43h)	3	4d05h	0.43
		6	13h02m	3.3
		9	4h20m	9.9
		12	1h35m	27
		18	33m	78
		24	11m	230
		36	3m	860
		48	81s	1 900
		72	29s	5 300
		96	10s	15 000
		114	3s	52 000

Table C.2: Computational performance for **cross-section** simulations for **reference melt pool** size.

Method:	Phase-Field	Cellular Automaton		
Hardware:	$2 \times \text{RTX2080Ti}$	$1 \times \text{Intel Xeon 6130 core (2.10 GHz)}$		
	Wall time	h_{CA}/h_{PF}	Wall time	Speed-up PF/CA
	2d11h	3	7d21h	0.31
	(59h)	6	1d00h	2.4
		9	8h10m	7.2
		12	3h25m	19
		18	1h08m	52
		24	26m	140
		36	10m	350
		48	3m	1 200
		72	58s	3 700
		96	19s	11 000
		114	6s	35 000

Table C.3: Computational performance for **cross-section** simulations for **wide & shallow melt pool** size.

Method:	Phase-Field	Cellular Automaton		
Hardware:	$2 \times \text{RTX3090}$	$1 \times \text{Intel Xeon 6130 core (2.10 GHz)}$		
	Wall time	h_{CA}/h_{PF}	Wall time	Speed-up PF/CA
	1d18h	3	2d05h	0.79
	(42h)	6	6h17m	6.7
		9	2h12m	19
		12	45m	56
		18	13m	190
		24	5m	500
		36	93s	1 600
		48	40s	3 800
		72	14s	11 000
		96	5s	30 000
		114	2s	76 000

Table C.4: Computational performance for **cross-section** simulations for **deep & narrow melt pool** size.

References

- [1] S.M. Elahi, R. Tavakoli, A.K. Boukellal, T. Isensee, I. Romero, D. Tourret, *Multiscale simulation of powder-bed fusion processing of metallic alloys*, Computational Materials Science 209, 111383 (2022).

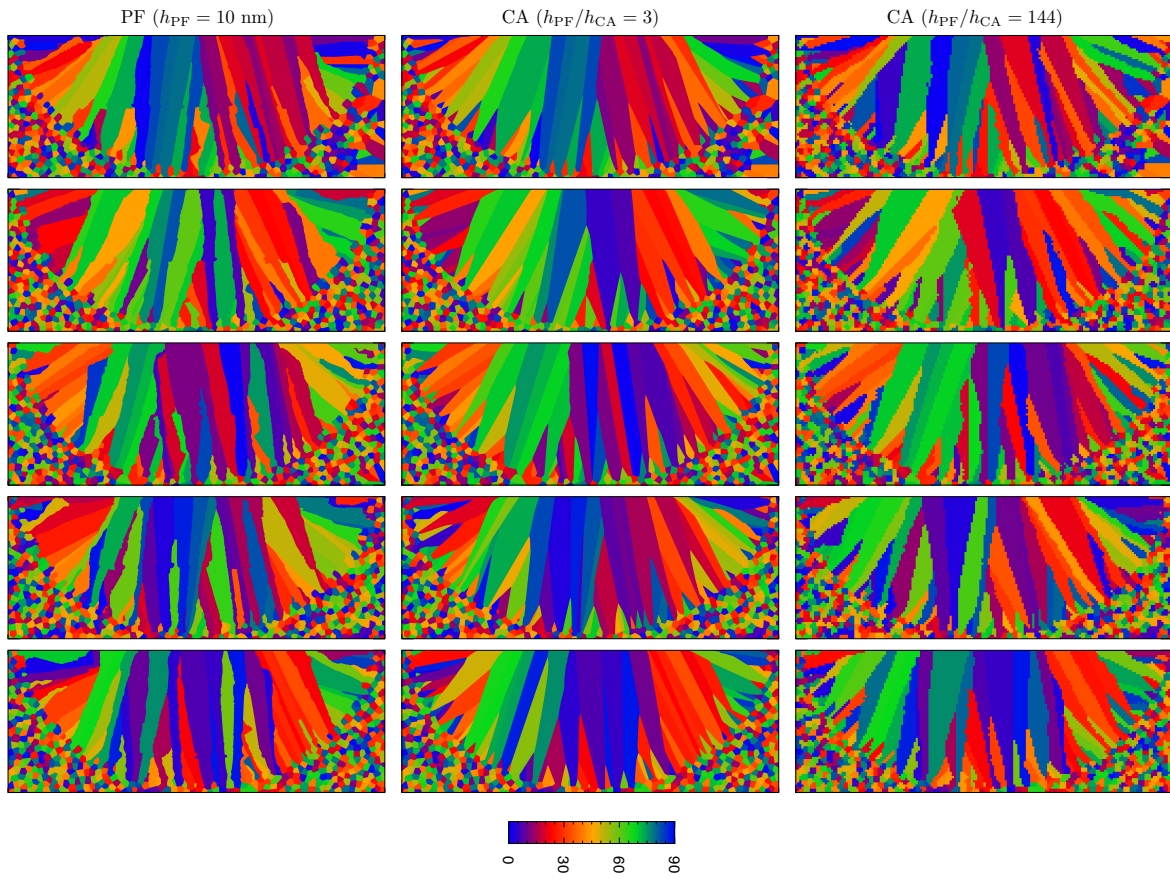


Figure C.1: Simulations of cross-section melt pool solidification for the reference case (i.e. thermal field as extracted from FE results) for five different initial grain distributions (rows) as predicted by phase-field (left column), and cellular automaton with fine (central column) and coarse (right column) spatial discretization. Domain size $\approx 257 \mu\text{m} \times 97 \mu\text{m}$.

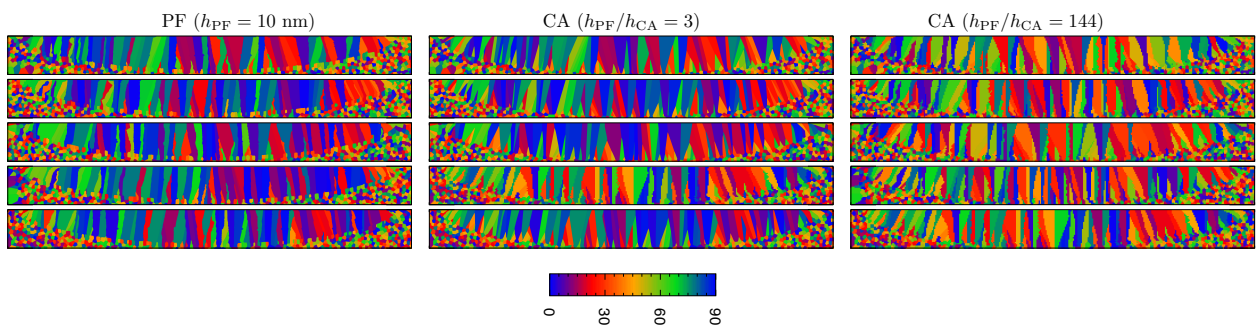


Figure C.2: Simulations of cross-section melt pool solidification for the reference case (i.e. thermal field as extracted from FE results) for five different initial grain distributions (rows) as predicted by phase-field (left column), and cellular automaton with fine (central column) and coarse (right column) spatial discretization. Domain size $\approx 513 \mu\text{m} \times 49 \mu\text{m}$.

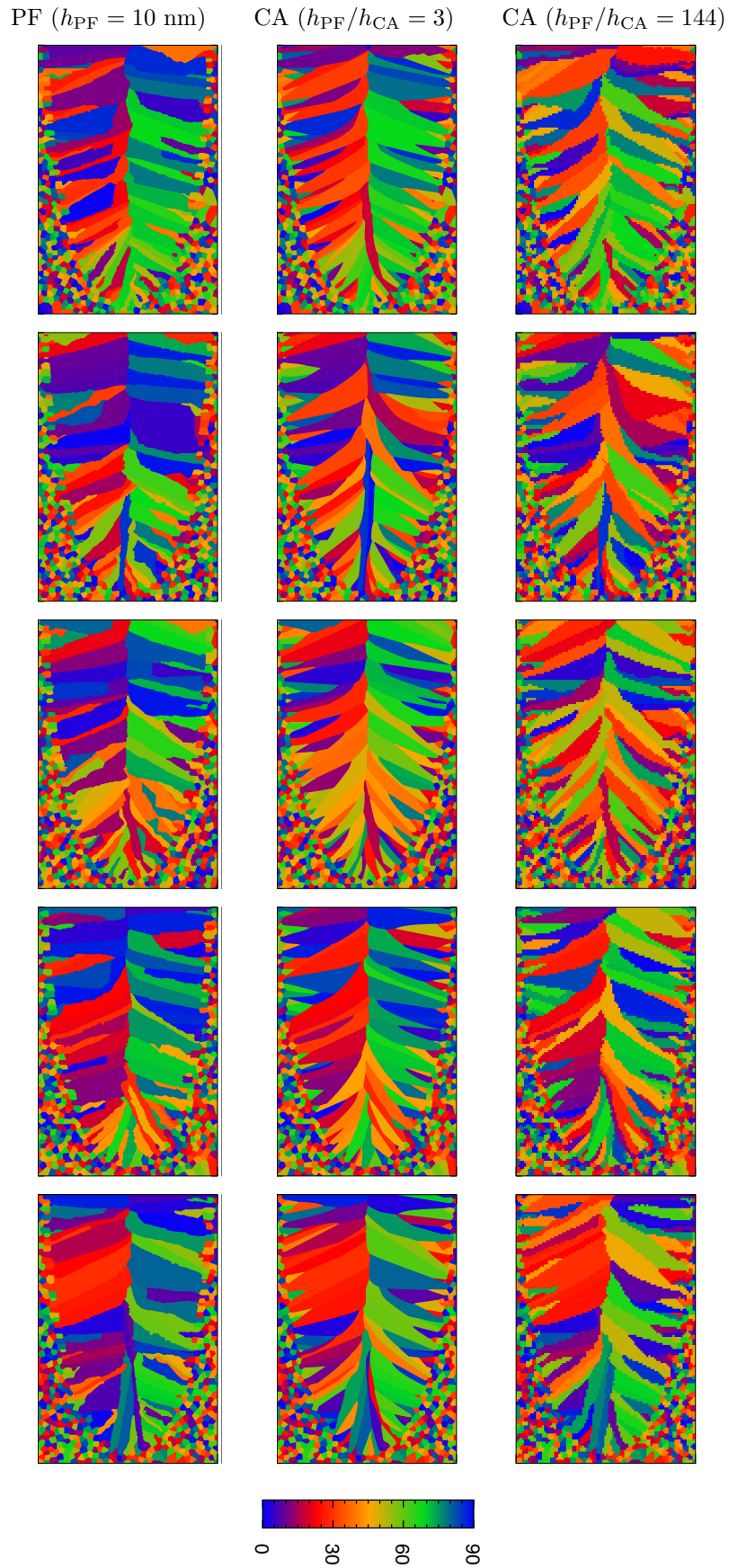


Figure C.3: Simulations of cross-section melt pool solidification of the deeper/narrower melt pool for five different initial grain distributions (rows) as predicted by phase-field (left column), and cellular automaton with fine (central column) and coarse (right column) spatial discretization. Domain size $\approx 129 \mu\text{m} \times 193 \mu\text{m}$.